CrystEngComm

Accepted Manuscript

ROYAL SOCIETY OF CHEMISTRY

www.rsc.org/crystengcomm

Table of Contents

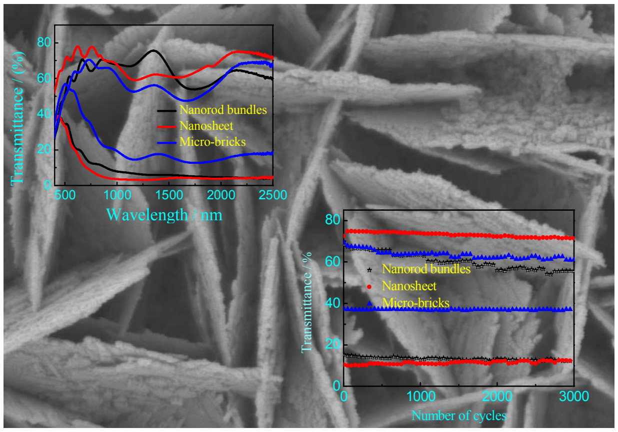

Vertically aligned hierarchical WO_3 nanosheet films are produced *via* a template-free and capping-agent-free hydrothermal method. The WO_3 nanosheet films exhibit a significant optical modulation, fast switching speed, high coloration efficiency and excellent cycling performance. Outstanding electrocatalytic ability for chemical reduction of H_2O_2 is also achieved by the films.

Direct growth of WO_3 nanosheet array on transparent conducting substrate for highly efficient electrochromic and electrocatalytic applications

Guo-fa Cai [1], Jiang-ping Tu *[1,2], Ding Zhou [1], Lu Li [1], Jia-heng Zhang [1], Xiu-li Wang[1,2] and Chang-dong Gu[1,2]

Author Address:[1] *State Key Laboratory of Silicon Materials, Key Laboratory of Advanced Materials and Applications for Batteries of Zhejiang Province, and Department of Materials Science and Engineering, Zhejiang University, Hangzhou 310027, China*

[2] *Cyrus Tang Center for Sensor Materials and Applications, Zhejiang University, Hangzhou 310027, China*

*Corresponding Author

Tel.: +86 571 87952856. Fax: +86 571 87952573.

E-mail: tujp@zju.edu.cn (J.P. Tu); tujplab@zju.edu.cn

Abstract

Vertically aligned hierarchical WO_3 nanosheet array on transparent conducting substrate is produced *via* a template-free and capping-agent-free hydrothermal method. Due to its high porosity among the nanosheets and good contact with the conductive substrate, the WO_3 nanosheet film exhibits advantageous electrochemical abilities. For example, a fast switching speed (5.2 and 2.2 s for coloration and bleaching, respectively), a significant optical modulation (62% at 633 nm, 67% at 2000 nm), a high coloration efficiency of 55.6 $cm^2\ C^{-1}$ at 700 nm and excellent cycling stability (95.4% after 3000 cycles) are achieved for the WO_3 nanosheet array film in electrochromic application. In addition, the nanosheet film also shows outstanding electrocatalytic ability for chemical reduction of H_2O_2.

1. Introduction

Tungsten trioxideis (WO_3) is an indirect band gap semiconductor and has been identified as one of the most promising inorganic working electrode materials for electrochromic, electrocatalytic, photocatalytic and sensing applications *etc,* because of its distinctive physical and chemical properties.[1–9] Electrochromism refers to the phenomenon that the optical properties can be switched reversibly and persistently in a material induced by an external voltage.[10–15] Electrochromic materials have received extensive attention in recent years since they could be effective candidates in various applications, such as large area information displays, rear-view mirrors for automobiles, smart windows and military camouflage.[16–25]

More recently, extensive efforts have been launched into the improvement of the electrochromic properties of inorganic oxides, such as coloration efficiency, response time, reversibility and stability. WO_3 has been identified as one of the most promising inorganic electrochromic materials due to its outstanding properties. The electrochromic phenomena of WO_3 are attributed to the injection/extraction of electrons and cations.[26–31] The kinetics and degree of ion insertion and the electrochromic reaction are limited by both the diffusion coefficient and the diffusion length of ions, because the rate-determining steps of ion intercalation and extraction are under diffusion control within a very thin surface layer of the host materials.[32–34] While the former depends on the crystal structure of metal oxide, the latter is determined by the architecture of electrode. Generally, nanostructured film can provide much more active reaction area and then lead to higher color contrast. In addition, the electrocatalytic properties of WO_3 are also based on the same injection/extraction of electrons and cations.[35] Therefore, a WO_3 film electrode with a porous structure and large active surface area is usually desired.

Generally, the approaches for producing nanostructured WO_3 films include electrodeposition,[36] hot-filament-assisted synthesis,[37] sputtering,[38] sol-gel [39] and hydrothermal processing.[40] Among these methods, hydrothermal process is promising for the production of WO_3 films because of its advantages, including low reaction temperatures, facility of control, cost saving and suitability for large-scale production, etc. The hydrothermal method has been used to synthesize one-dimensional (1D) WO_3 nanowires or nanorods.[41–43] Previously, our group had also prepared WO_3 nanowire on fluorine-doped tin oxide (FTO) glass [44] and WO_3 nanotree on tungsten foils [45] by the hydrothermal method with capping-agent. However, because of the poor contact between the WO_3 nanowires and the transparent conductive substrate, the active surface area of the nanostructures was not sufficiently utilized due to the compact stacking which affected the response speed and the coloration efficiency. Therefore, to establish a facile preparation method for the structural control of WO_3 thin films, as well as to expound the relationship between distinct nanostructures and their electrochromic properties is of high importance in the field of electrochromism. Recently, materials with sheet structure are one of the most promising electrode materials owing to their large surface area and high electrical conductivity. For instance, two dimensional graphene and some oxide nanosheets were extensively investigated by some researchers. [46–49] To the best of our knowledge, most reports dedicated to research WO_3 nanosheet films synthesized by solvothermal or adding capping agent methods.[50–53] However, there have been no reports on the preparation of WO_3 nanosheet films by hydrothermal method at different pH values. Herein, we make an attempt to grow vertically aligned WO_3 nanosheets directly on FTO-coated glass by a simple hydrothermal approach. Two-dimension WO_3 nanosheet array on transparent conducting substrate may prove to be a promising material for electrochromism and electrocatalysis due to their unique features including high optical transparency and highly porous space among the nanosheets. We investigated the effects of initial pH value of the hydrothermal process on the nanostructures of the obtained WO_3 films. We also discussed the electrochromic properties and the electrocatalytic ability for hydrogen peroxide oxidation (H_2O_2) of the WO_3 films.

2. Experiments and methods

All chemicals used in this work were of analytical grade and purchased from Sinopharm Chemical Reagent Co., Ltd. (China) and used as received. Unless specified, all solutions were prepared using de-ionized water.

2.1 Preparation of WO_3 films

Before hydrothermal growth, a WO_3 seed layer was deposited on a FTO coated glass substrate through spin coating. Firstly, the FTO-coated glass (2×4 cm^2 in size) was washed with acetone, ethanol, and de-ionized water in an ultrasonic bath for 10 min, respectively, and then blow-dried with nitrogen gas. The WO_3 sol was prepared by dissolving 0.5 g H_2WO_4 into 100 ml H_2O and adding 30 mL H_2O_2 with stirring for 8 h, and then the sol was cast onto the FTO-coated glass through spin coating technology. The spin coating process was performed at 3000 rpm for 30 s and repeated for 4 times. Subsequently, the WO_3 sol-coated substrates were heated to 400°C in air for 40 min.

WO_3 films were fabricated by a typical synthesis process. Briefly, 3.29 g sodium tungstate powder was dissolved in 76 ml de-ionized water, and then different amount of HCl was added to the reaction precursor to adjust the pH values to 2.0, 1.5 and 0.5, respectively. After stirring for 1 h, the obtained solutions were transferred into a Teflon lined stainless autoclave. The FTO-coated glass with the WO_3 seed layer was placed vertically in the autoclave, and then the autoclave was sealed and heated at 200°C for 70 min. After synthesis, the autoclave was cooled to room temperature under flowing water, for approximately 20 min. Afterwards, the as-deposited films were washed and dried in a vacuum oven (9×10^{-2} MPa) at 60 °C for 12 h.

2.2 Characterization

The crystal structure and morphology of WO_3 films were investigated using X-ray diffraction (XRD, RIGAKU D/MAX 2550/PC with Cu Kα radiation), X-ray photoelectron spectroscopy (XPS, Thermo Scientific ESCALAB 250Xi equipped with a dual Mg Kα-Al Kα anode for photo excitation), field emission scanning electron microscopy (FESEM, Hitachi SU-70) and transmission electron microscopy (TEM, FEI tecnai G2 F20). The transmission spectra of the electrochromic films in the fully colored and fully bleached states were carried out on a SHIMADZU UV-3600 spectrophotometer over the wavelength range from 400 to 2500 nm at room temperature. The electrochromic properties of the WO_3 films were conducted on a

CHI660D electrochemical workstation using a three-electrode electrochemical cell with 0.5 M H_2SO_4 as the electrolyte, platinum foil as the counter- electrode and Ag/AgCl as the reference electrode. The electrocatalytic ability of the WO_3 films for H_2O_2 was also performed on this electrochemical workstation.

3. Results and discussion

3.1 Structure and morphology

The structural evolution of the WO_3 films as a function of pH value was studied by XRD analysis. After subtracting the diffraction peaks of FTO glass, it is confirmed from Fig. 1 that all the films are well indexed to the standard diffraction pattern of hexagonal WO_3 (JCPDS No. 75-2187). The sharp peaks also indicate that the WO_3 films are crystallized. In addition, the relative peak intensities for crystalline planes of (001) and (200) of the films are obviously different, revealing different preferred growing direction due to the effect of pH value.

XPS measurement was performed to investigate the oxidation state of WO_3. Fig. 2 shows the W 4f core-level XPS spectrum of WO_3 film. There are spin–orbit doublets in this spectrum corresponding to W $4f_{7/2}$, W $4f_{5/2}$ and W $5p_{3/2}$ peaks which are located at 35.6 eV, 37.6 eV and 41.5 eV, respectively. These values match well with those reported in the literatures.[54–57] It can be reasoned that W in the films is at the highest oxidation state (W^{6+}).

The SEM images of the WO_3 films synthesized at different pH values are shown in Fig. 3. It can be clearly seen that the surface morphology of the obtained WO_3 films on the FTO substrate varies with the pH value of the hydrothermal solutions. When the pH value is fixed at 2.0, the main products are bundles which are composed of large number nanorods vertical to FTO substrate, and the average length of each bundle is about 500 nm (Fig. 3a-b). When the pH value is adjusted to 1.0, the WO_3 film is composed of nanosheets and the sheets are about 10–15 nm in thicknesses (Fig. 3c-d). Numerous pores are formed among the nanosheets so that the ions in the electrolyte can diffuse more easily and efficiently. As the pH value is decreased to 0.5, the WO_3 film is composed of bulk micro-bricks and some thick tetragonal nanorods with square top facets (Fig. 3e-f). The thicknesses of all the WO_3 films are about 500 nm, as shown in the insets of Fig. 3. The precipitation of WO_3 from a tungstate ion solution using concentrated acid is a well-known synthetic route described as follows:

$$Na_2WO_4 + 2HCl + nH_2O \rightarrow H_2WO_4{\cdot}nH_2O + 2NaCl \quad (1)$$

$$H_2WO_4{\cdot}nH_2O \xrightarrow{\text{hydrothermal}} WO_3 + (n+1)\ H_2O \quad (2)$$

The pH value is a critical parameter for governing the numbers of the WO_3 nuclei and the formation rate of WO_3 nanostructures. When the pH value is fixed at 2.0, less crystal nuclei are generated, which favor the subsequent growth. As a result, the primary products are WO_3 bundles which are composed of large numbers of nanorods. When the pH value is fixed at 1.0 with the increase of H^+ concentration, a great number of small WO_3 nuclei are quickly generated, leading to lots of parallel arranged nanowires. Moreover, the parallel nanowires interlace with one another to form a nanosheet structure. When the final pH value is down to 0.5, both nuclei and the formation rate are fast, the film is totally compacted which composed of bulk micro-bricks and some thick tetragonal nanorods.

The structural characteristics of the WO_3 nanosheet are further investigated by TEM analysis, as shown in Fig. 4. From the low magnification image (Fig. 4a), the WO_3 nanosheet presents thin layered structure. The high magnification image exhibits clear lattice fringes, and the spacing between adjacent lattice planes is 0.389 nm corresponding to the (001) planes of hexagonal WO_3, indicating that the nanosheet is pure WO_3 (Fig. 4b).

3.2. Electrochemical and electrochromic properties

Fig. 5 shows the cyclic voltammogram (CV) of WO_3 films measured in 0.5 M H_2SO_4 at a sweep rate of 20 mV s^{-1}. Just one redox process is seen in the CV curve, which can be ascribed to intercalation (deintercalation) of H^+ into (out from) the WO_3. This intercalation (deintercalation) process can be described as:

$$WO_3 + xH^+ + xe^- \leftrightarrow H_xWO_3 \qquad (3)$$

All of the CVs were normalized to the geometric area of the electrode, resulting in units of mA cm^{-2}. The area of the hysteresis curves and the position of anodic and cathodic peaks are closely related to the electrochemical processes occurring in the electrochromic films. It is observed that the cathodic and anodic current densities of the WO_3 nanorod bundle and nanosheet array electrodes are larger than those of the WO_3 micro-brick electrode. The increase in the area of voltammograms suggests that the vertically aligned nanorod bundles and nanosheets offer an easy way for diffusion and charge transfer process of ions in the WO_3 film.

Fig. 6 shows the visible and near-infrared transmittance spectra of the WO_3 films in the colored and bleached states measured in the wavelength range of 400–2500 nm under different potentials. Generally, when the WO_3 films were cathodically polarized, they had a very uniform blue color, which intensified with increasing cathodic potential. When the blue films were anodically polarized, they were bleached and transparent. It can be seen from Fig. 6 that the porous WO_3 nanosheet array presents noticeable electrochromism with variation of transmittance up to 62% at 700 nm and 67% at 2000 nm, respectively. However, the modulation ranges of the transmittance are 53% and 32% at 700 nm, 56%, and 45% at 2000 nm for the WO_3 nanorod bundles and WO_3 micro-bricks, respectively. The transmittance modulation value of 62% at 700 nm is comparable to those WO_3 nano-porous networks obtained from the anodization method,[58] but much higher than that of WO_3 nanorod bundles, WO_3 micro-bricks and others obtained WO_3 nanosheets.[59,60] The photographs of the sample in the colored and bleached states are shown in Fig. 7.

An important aspect of electrochromism is the temporal response under alternating potentials. The color switching times of the WO_3 films are investigated by chronoamperometry (CA), and the corresponding in situ coloration/bleaching transmittance response at a wavelength of 700 nm with alternately applying potential between −0.7 V and 1.0 V are shown in Fig. 8. The switching time is defined as the time required for 90% change in the transmittance between the bleached and colored states. For the WO_3 nanosheet array, the coloration time (from the bleached state to the colored state) t_c is found to be 5.2 s, and the bleaching time (from the colored state to the bleached state) t_b is 2.2 s. The color switching time of the WO_3 nanosheet array is faster than those of the WO_3 nanorod bundle and micro-brick films. The latter WO_3 nanorod bundles and micro-bricks take longer t_c / t_b of 6.4/6.5 s and 7.8/16.4 s, respectively. The fast switching speed of the WO_3 nanosheet array film is attributed to the porous space among the nanosheets, which makes the ion diffusion easier and the active surface area can be sufficiently utilized for charge-transfer reactions.

One of the most important criteria for comparing different electrochromic materials is its coloration efficiency (*CE*). *CE* is defined as the change in optical density (ΔOD) per unit of charge (ΔQ) intercalated into the electrochromic layers. Both ΔOD and *CE* present the ability of optical modulation during the coloration-bleaching process, but the *CE* is under the considering of energy consumption. Generally, a high value of *CE* indicates that the electrochromic materials exhibit a large optical modulation with a small intercalation charge density. It can be calculated from the following formulas: [61,62]

$$CE(\lambda)=\frac{\Delta OD(\lambda)}{\Delta Q} \quad (4)$$

$$\Delta OD(\lambda)=\log\frac{T_{\mathrm{b}}}{T_{\mathrm{c}}} \quad (5)$$

where T_b and T_c refers to the transmittance in bleached and colored states, respectively. Fig. 9 shows the plots of ΔOD at a wavelength of 700 nm versus the inserted charge density at a potential of −0.7 V. The *CE* value is calculated to be 55.6 $cm^2\ C^{-1}$ at 700 nm for the WO_3 nanosheet array, which is higher than that of WO_3 nanorod bundles and micro-bricks. Combining the results of switching characteristics shown in Fig. 8, it can be concluded that, for the WO_3 nanosheet array film, a major optical modulation is completed in a short time after voltage switching. The result indicates that the improvement in *CE* value of the WO_3 nanosheet array is attributed to the more open space among the nanosheets and good contact between the nanosheet and the substrate. It provides a larger surface area for charge-transfer reactions.

The electrochemical stability of the WO_3 films was measured by CA measurements at 700 nm under a square wave potential oscillating between −0.7 and 1.0 V for 3000 cycles. It can be seen from Fig. 10 that the WO_3 nanosheet array film sustains a transmittance modulation of about 95.4% after subjected for 3000 cycles. However, the WO_3 nanorod bundle and micro-brick films only sustain a transmittance modulation of about 82.1% and 75.0 % after 3000 cycles. Excellent cycling durability of the nanosheet array film can be attributed to the effect of its structure. The vertically aligned WO_3 nanosheets show strong degree of adhesion to the FTO glass substrate, which leads to a slow degeneration in electrolyte solution. In addition, the WO_3 nanosheet array film possesses a high *CE* which can provide a large transmittance modulation by a small change in the amount of intercalated cations. Thereby, it would result in a good reliability due to the less charge needed for coloration/bleaching.

The above results demonstrate that the vertically aligned WO_3 nanosheet exhibits highly efficient electrochromic properties. In addition, we envisioned that the WO_3 nanosheet films could have outstanding properties in electrocatalysis. H_2O_2, a well-known oxidizing agent, is not only a by-product of a large number of oxidase enzymes, but also an essential intermediate in physiological processes, food production, pharmaceutical, industrial and environmental fields. [63–65] Therefore, it is of great significance to develop electrocalalysts with highly-selective H_2O_2 sensing property with fast and sensitive responses. Fig.11 displays the CV profiles of WO_3 films in 0.5 M H_2SO_4 and 0.025 M H_2O_2 solution at a scanning rate of 20 mV s^{-1}. A sharp decrease in the cathode current density for the chemical reduction of H_2O_2 by electrogenerated tungsten bronzes is noticed. The mechanism of chemical reduction of H_2O_2 on WO_3 films may be simply illustrated by reaction (3) and the following reaction: [66]

$$2H_xWO_3 + xH_2O_2 \leftrightarrow 2WO_3 + 2x\,H_2O \qquad (6)$$

Pure FTO electrode shows almost no electrochemical reaction for chemical reduction of H_2O_2. The WO_3 nanosheet film has 1.5 times larger specific activity values than that of the WO_3 micro-bricks. These results present great promise for the WO_3 nanosheet film as a practical electrocatalytic material.

4. Conclusions

The vertically aligned WO_3 nanosheet film has been successfully prepared on a FTO-coated glass. Compared to the nanorod bundles and micro-bricks, the nanosheet array exhibits highly enhanced ion insertion and electrochromic properties with higher coloration efficiency, faster switching speed, larger optical modulation and more excellent cycling stability. The WO_3 nanosheet array also demonstrat extraordinary electrocatalytic ability for chemical reduction of H_2O_2. The improved electrochemical properties are mainly due to the porous space among the nanosheets and good contact between the array and the substrate, which makes the diffusion of ions easier and provides larger active surface area for charge-transfer reactions.

Acknowledgments

This work was supported by the Program for Innovative Research Team in University of Ministry of Education of China (IRT13037), Key Science and Technology Innovation Team of Zhejiang Province (2010R50013) and a support program of the Ministry of Education of China.

References

1. C.-G. Granqvist, *Nat. Mater.*, 2006, **5**, 89.
2. H. Zheng, J. Z. Ou, M. S. Strano, R. B. Kaner, A. Mitchell and K. Kalantar-zadeh, *Adv. Funct. Mater.*, 2011, **21**, 2175.
3. G. F. Cai, D. Zhou, Q. Q. Xiong, J. H. Zhang, X. L. Wang, C. D. Gu and J. P. Tu, *Sol. Energy Mater. Sol. Cells*, 2013, **117**, 231.
4. F. Zheng, H. Lu, M. Guo and M. Zhang, *CrystEngComm*, 2013, **15**, 5828.
5. Z. Xie, Y. G. Zhu, J. Xu, H. T. Huang, D. Chen and G. Z. Shen, *CrystEngComm*, 2011, **13**, 6393.
6. A. Phuruangrat, D. J. Ham, S. J. Hong, S. Thongtem and J. S. Lee, *J. Mater. Chem.*, 2010, **20**, 1683.
7. H. B. Zhang, M. S. Yao, L. Y. Bai, W. C. Xiang, H. C. Jin, J. L. Li and F. L. Yuan, *CrystEngComm*, 2013, **15**, 1432.
8. J. Y. Li, J. F. Huang, J. P. Wu, L. Y. Cao, Q. J. Li and K. Yanagisawa, *CrystEngComm*, 2013, **15**, 7904.
9. C. Santato, M. Odziemkowski, M. Ulmann and J. Augustynski, *J. Am. Chem. Soc.*, 2001, **123**, 10639.
10. C. G. Granqvist, *J. Eur. Ceram. Soc.*, 2005, **25**, 2907.
11. G. F. Cai, J. P. Tu, C. D. Gu, J. H. Zhang, J. Chen, D. Zhou, S. J. Shi and X. L. Wang, *J. Mater. Chem. A*, 2013, **1**, 4286.
12. J. Zhang, J. P. Tu, G. F. Cai, G. H. Du, X. L. Wang and P. C. Liu, *Electrochim. Acta*, 2013, **99**, 1.

13. F. Lin, J. Cheng, C. Engtrakul, A. C. Dillon, D. Nordlund, R. G. Moore, T.-C. Weng, S. K. R. Williams and R. M. Richards, *J. Mater. Chem.*, 2012, **22**, 16817.

14. C. M. Lampert, *Mater. Today*, 2004, **7**, 28.

15. G. F. Cai, C. D. Gu, J. Zhang, P. C. Liu, X. L. Wang, Y. H. You and J. P. Tu, *Electrochim. Acta*, 2013, **87**, 341.

16. C. G. Granqvist, *Adv. Mater.*, 2003, **15**, 1789.

17. G. F. Cai, J. P. Tu, J. Zhang, Y. J. Mai, Y. Lu, C. D. Gu and X. L. Wang, *Nanoscale*, 2012, **4**, 5724.

18. Z. J. Yao, J. T. Di, Z. Z. Yong, Z. G. Zhao and Q. W. Li, *Chem. Commun.*, 2012, **48**, 8252.

19. C. M. Lampert, *Sol. Energy Mater. Sol. Cells*, 2003, **76**, 489.

20. X. H. Xia, J. P. Tu, J. Zhang, X. L. Wang, W. K. Zhang and H. Huang, *Electrochim. Acta*, 2008, **53**, 5721.

21. G. F. Cai, J. P. Tu, D. Zhou, J. H. Zhang, Q. Q. Xiong, X. Y. Zhao, X. L. Wang and C. D. Gu, *J. Phys. Chem. C*, 2013, **117**, 15967.

22. G. F. Cai, J. P. Tu, D. Zhou, X. L. Wang and C. D. Gu, *Sol. Energy Mater. Sol. Cells*, 2014, **124**, 103.

23. Y. X. Lu, L. Liu, D. Mandler and P. S. Lee, *J. Mater. Chem. C*, 2013, **1**, 7380.

24. J. Zhang, J. P. Tu, D. Zhang, Y. Q. Qiao, X. H. Xia, X. L. Wang and C. D. Gu, *J. Mater. Chem.*, 2011, **21**, 17316.

25. Z. C. Wang and X. F. Hu, *Electrochim. Acta*, 2001, **46**, 1951.

26. A. E. Aliev and H. W. Shin, *Solid State Ionics*, 2002, **154–155**, 425.

27. S. H. Baeck, K. S. Choi, T. F. Jaramillo, G. D. Stucky and E. W. McFarland, *Adv. Mater.*, 2003, **15**, 1269.

28. J. Zhang, X. L. Wang, X.H. Xia, C. D. Gu, Z. J. Zhao and J. P. Tu, *Electrochim. Acta*, 2010, **55**, 6953.

29. S. Sallard, T. Brezesinski and B. M. Smarsly, *J. Phys. Chem. C*, 2007, **111**, 7200.

30. J.-W. Liu, J. Zheng, J.-L. Wang, J. Xu, H.-H. Li and S.-H. Yu, *Nano Lett.*, 2013, **13**, 3589.

31. J. M. Wang, E. Khoo, P. S. Lee and J. Ma, *J. Phys. Chem. C*, 2008, **112**, 14306.

32. D. Y. Ma, G. Y. Shi, H. Z. Wang, Q. H. Zhang and Y. G. Li, *J. Mater. Chem.A*, 2013, **1**, 684.

33. S. H. Lee, R. Deshpande, P. A. Parilla, K. M. Jones, B. To, A. H. Mahan and A. C. Dillon, *Adv. Mater.*, 2006, **18**, 763.

34. Y.-Y. Song, Z.-D. Gao, J.-H. Wang, X.-H. Xia and R. Lynch, *Adv. Funct. Mater.*, 2011, **21**, 1941.

35. V. K. Laurinavichyute, A. A. Khokhlov, S. Y. Vassiliev, A. V. Vannikov and G. A. Tsirlina, *Electrochim. Acta*, 2013, **99**, 102.

36. T. Pauporté, *J. Electrochem. Soc.*, 2002, **149**, C539.

37. J. Thangala, S. Vaddiraju, R. Bogale, R. Thurman, T. Powers, B. Deb and M. K. Sunkara, *Small*, 2007, **3**, 890.

38. A. Karuppasamy, *Appl. Surf. Sci.*, 2013, **282**, 77.

39. N. Naseri, R. Azimirad, O. Akhavan and A. Z. Moshfegh, *Thin Solid Films*, 2010, **518**, 2250.

40. F. Zheng, M. Guo and M. Zhang, *Crystengcomm*, 2013, **15**, 277.

41. J. M. Wang, E. Khoo, P. S. Lee and J. Ma, *J. Phys. Chem. C*, 2009, **113**, 9655.

42. G. F. Cai, X. L. Wang, D. Zhou, J. H. Zhang, Q. Q. Xiong, C. D. Gu and J. P. Tu, *RSC Adv.*, 2013, **3**, 6896.

43. S. S. Kalanur, Y. J. Hwang, S. Y. Chae and O. S. Joo, *J. Mater. Chem. A*, 2013, **1**, 3479.

44. J. Zhang, J. P. Tu, X. H. Xia, X. L. Wang and C. D. Gu, *J. Mater. Chem.*, 2011, **21**, 5492.

45. J. Zhang, X. L. Wang, X. H. Xia, C. D. Gu and J. P. Tu, *Sol. Energy Mater. Sol. Cells*, 2011, **95**, 2107.

46. A. K. Geim, *Science*, 2009, **324**, 1530.

47. J. T. Li, W. Zhao, F. Q. Huang, A. Manivannan and N. Q. Wu, *Nanoscale*, 2011, **3**, 5103.

48. J. W. Ma, S. Su, W. Y. Fu, H. B. Yang, X. M. Zhou, H. Z. Yao, Y. L. Chen, L. H. Yang, M. L. Sun, Y. N. Mu and P. Lv, *CrystEngComm*, 2014, **16**, 2910.

49. Y. Shi, J. Z. Wang, S. L. Chou, D. Wexler, H. J. Li, K. Ozawa, H. K. Liu and Y. P. Wu, *Nano Lett.*, 2013, **13**, 4715.

50. F. Amano, D. Li and B. Ohtani, *Chem. Commun.*, 2010, **46**, 2769.

51. J. Su, X. Feng, J. D. Sloppy, L. Guo and C. A. Grimes, *Nano Lett.*, 2010, **11**, 203.

52. Z. H. Jiao, X. Wang, J. M. Wang, L. Ke, H. V. Demir, T. W. Koh and X. W. Sun, *Chem. Commun.*, 2012, **48**, 365.

53. Z. H. Jiao, J. M. Wang, L. Ke, X. W. Sun and H. V. Demir, *ACS Appl. Mater. Interfaces*, 2011, **3**, 229.

54. L. Yang, D. Ge, J. Zhao, Y. Ding, X. Kong and Y. Li, *Sol. Energy Mater. Sol. Cells*, 2012, **100**, 251.

55. H.-C. Lin, C.-Y. Su, Y.-H. Yu and C.-K. Lin, *J. Nanopart. Res.*, 2012, **14**, 1.

56. S. Komornicki, M. Radecka and P. Sobas, *J. Mater. Sci.-Mater. Electron.*, 2004, **15**, 527.

57. V. I. Bukhtiyarov, *Catal. Today*, 2000, **56**, 403.

58. J. Z. Ou, S. Balendhran, M. R. Field, D. G. McCulloch, A. S. Zoolfakar, R. A. Rani, S. Zhuiykov, A. P. O'Mullane and K. Kalantar-zadeh, *Nanoscale*, 2012, **4**, 5980.

59. K. Wang, P. Zeng, J. Zhai and Q. Liu, *Electrochem. Commun.*, 2013, **26**, 5.

60. L. Liang, J. J. Zhang, Y. Y. Zhou, J. F. Xie, X. D. Zhang, M. Guan, B. C. Pan and Y. Xie, *Sci. Rep.*, 2013, **3**, Art. 1936.

61. L. C. Chen and K. C. Ho, *Electrochim. Acta*, 2001, **46**, 2151.

62. C. G. Granqvist, S. Green, G. A. Niklasson, N. R. Mlyuka, S. von Kræmer and P. Georén, *Thin Solid Films*, 2010, **518**, 3046.

63. Y. Zhang, X. Bo, A. Nsabimana, C. Luhana, G. Wang, H. Wang, M. Li and L. Guo, *Biosens. Bioelectron.*, 2014, **53**, 250.

64. M. Kang, Y. Yang, J. H. Shim, S. C. Lee, Y. Lee and C. Lee, *Electroanalysis*,

2013, **25**, 2691.

65. S.-H. Chang, M.-H. Yeh, J. Rick, W.-N. Su, D.-G. Liu, J.-F. Lee, C.-C. Liu and B.-J. Hwang, *Sensors Actuat. B-Chem.*, 2014, **190**, 55.

66. H. Razmi and R. Mohammad-Rezaei, *Electrochim. Acta*, 2011, **56**, 7220.

Figure captions

Fig. 1 XRD patterns of WO_3 films: (a) pH = 2.0, (b) pH = 1.0, (c) pH = 0.5.

Fig. 2 XPS spectra film of W 4f for the WO_3 nanosheet array.

Fig. 3 SEM images WO_3 films of (a) and (b) pH = 2.0, (c) and (d) pH = 1.0, (e) and (f) pH = 0.5 (cross sectional view presented in inset).

Fig. 4 TEM image of (a) the WO_3 nanosheet array scratched from the FTO substrate, (b) HRTEM image of the WO_3 nanosheet.

Fig. 5 Cyclic voltammograms of WO_3 films on FTO glass as working electrode in 0.5 M H_2SO_4 at a scan rate of 20 mV s^{-1} in the potential range of −0.7 to 1.0 *vs*. Ag/AgCl. The redox pair shows the H^+ insertion into and releasing from the WO_3 film.

Fig. 6 Visible and near-infrared transmittance spectra of WO_3 films at their colored and bleached states.

Fig. 7 Photographs of a WO_3 nanosheet array sample (2×4 cm^2 in size) under different applied potentials.

Fig. 8 (a) Current responses for WO_3 films at −0.7 and 1.0 V applications for 30 s per step, (b) corresponding in situ optical responses of WO_3 films for 30 s per step measured at 700 nm.

Fig. 9 Variation of the in situ optical density (*OD*) vs. charge density for the films.

Fig. 10 Durability test of the WO_3 films for 3000 cycles.

Fig. 11 CV curves of WO_3 films measured in 0.5 M H_2SO_4 and 0.025 M H_2O_2 solution at a scanning rate of 20 mV s^{-1}.

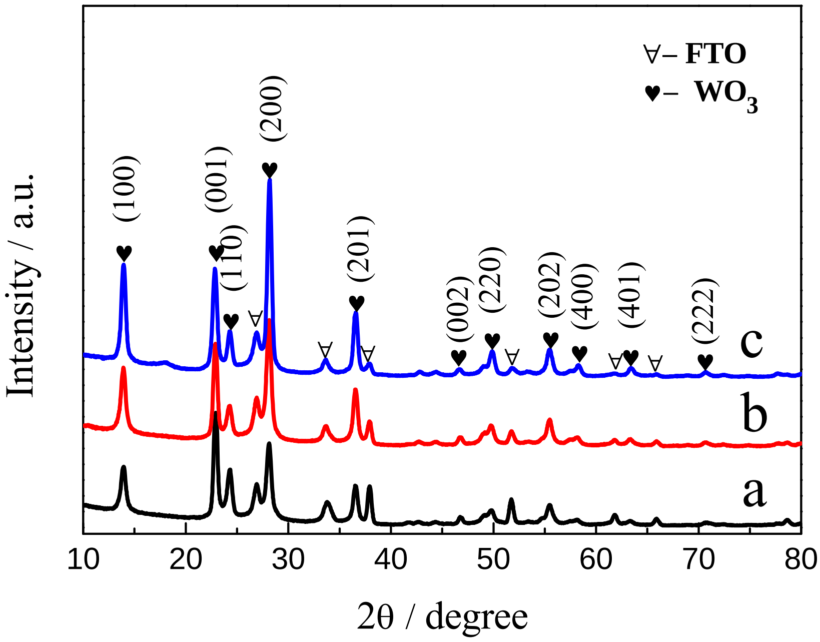
∀– FTO
♥– WO3
(100)
(001)
(110)
(200)
(201)
(002)
(220)
(202)
(400)
(401)
(222)
c
b
a
Intensity / a.u.
10
20
30
40
50
60
70
80
2θ / degree

Fig. 1

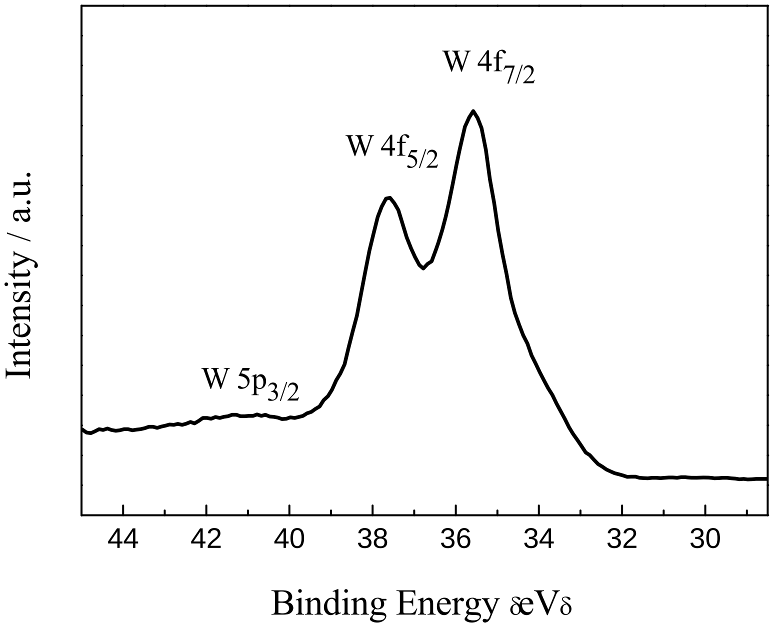
W 4f7/2
W 4f5/2
W 5p3/2
Intensity / a.u.
44
42
40
38
36
34
32
30
Binding Energy ǽVǼ

Fig. 2

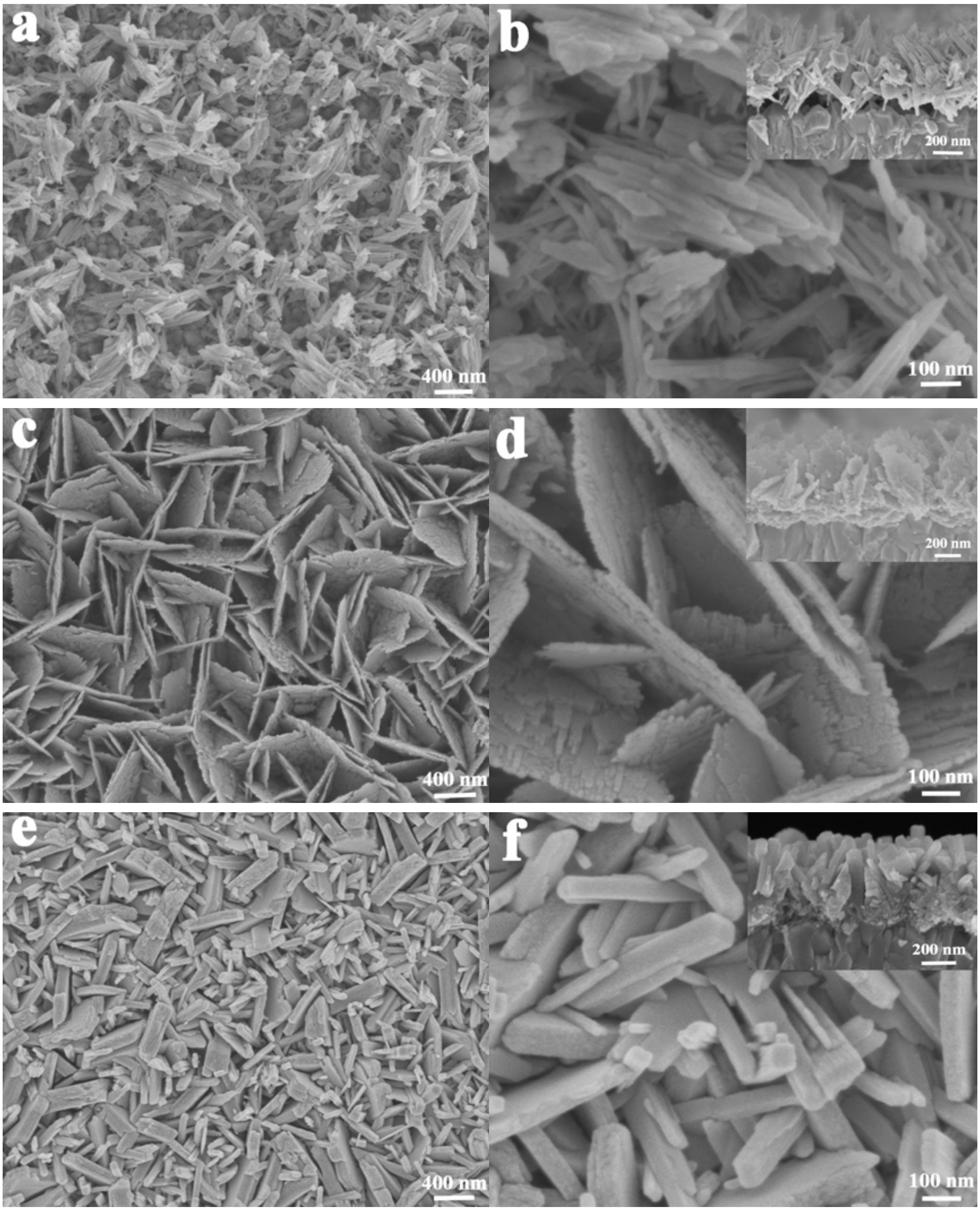
a
400 nm
b
200 nm
100 nm
c
400 nm
d
200 nm
100 nm
e
400 nm
f
200 nm
100 nm

Fig. 3

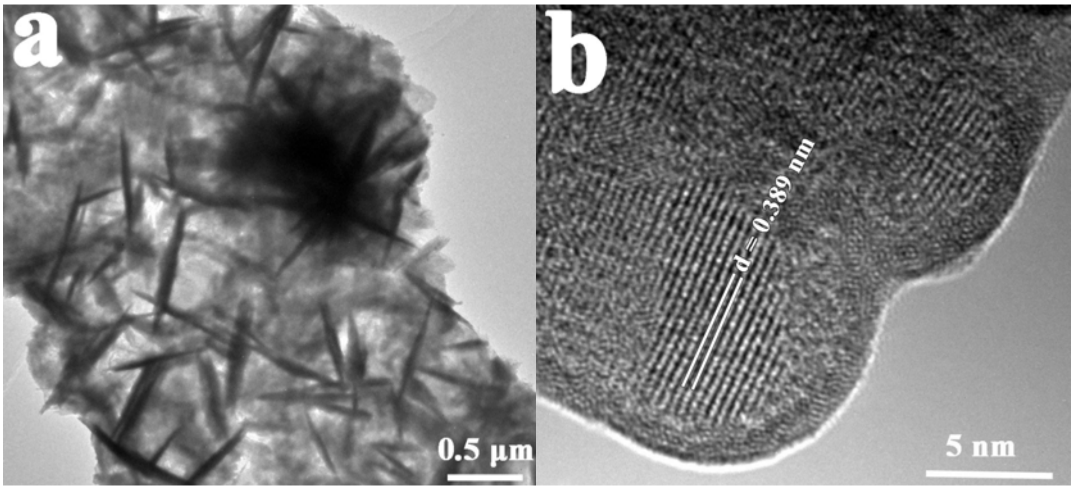

Fig. 4

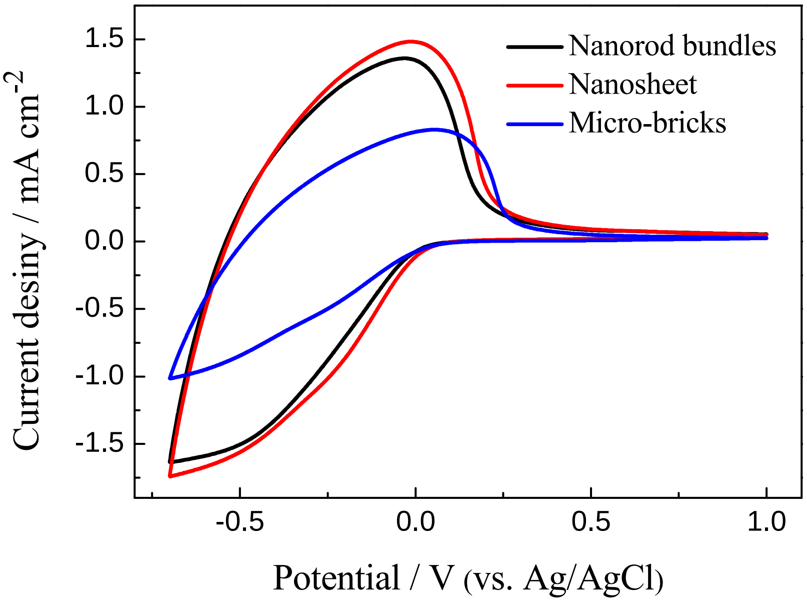
Nanorod bundles
Nanosheet
Micro-bricks
Current desiny / mA cm^{-2}
1.5
1.0
0.5
0.0
-0.5
-1.0
-1.5
-0.5
0.0
0.5
1.0
Potential / V (vs. Ag/AgCl)

Fig. 5

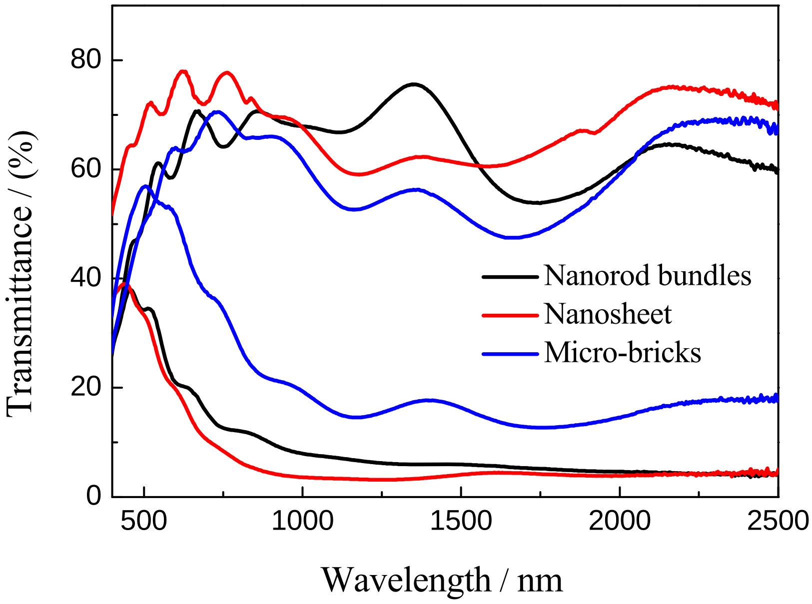
Transmittance / (%)
0
20
40
60
80
500
1000
1500
2000
2500
Wavelength / nm
Nanorod bundles
Nanosheet
Micro-bricks

Fig. 6

Fig. 7

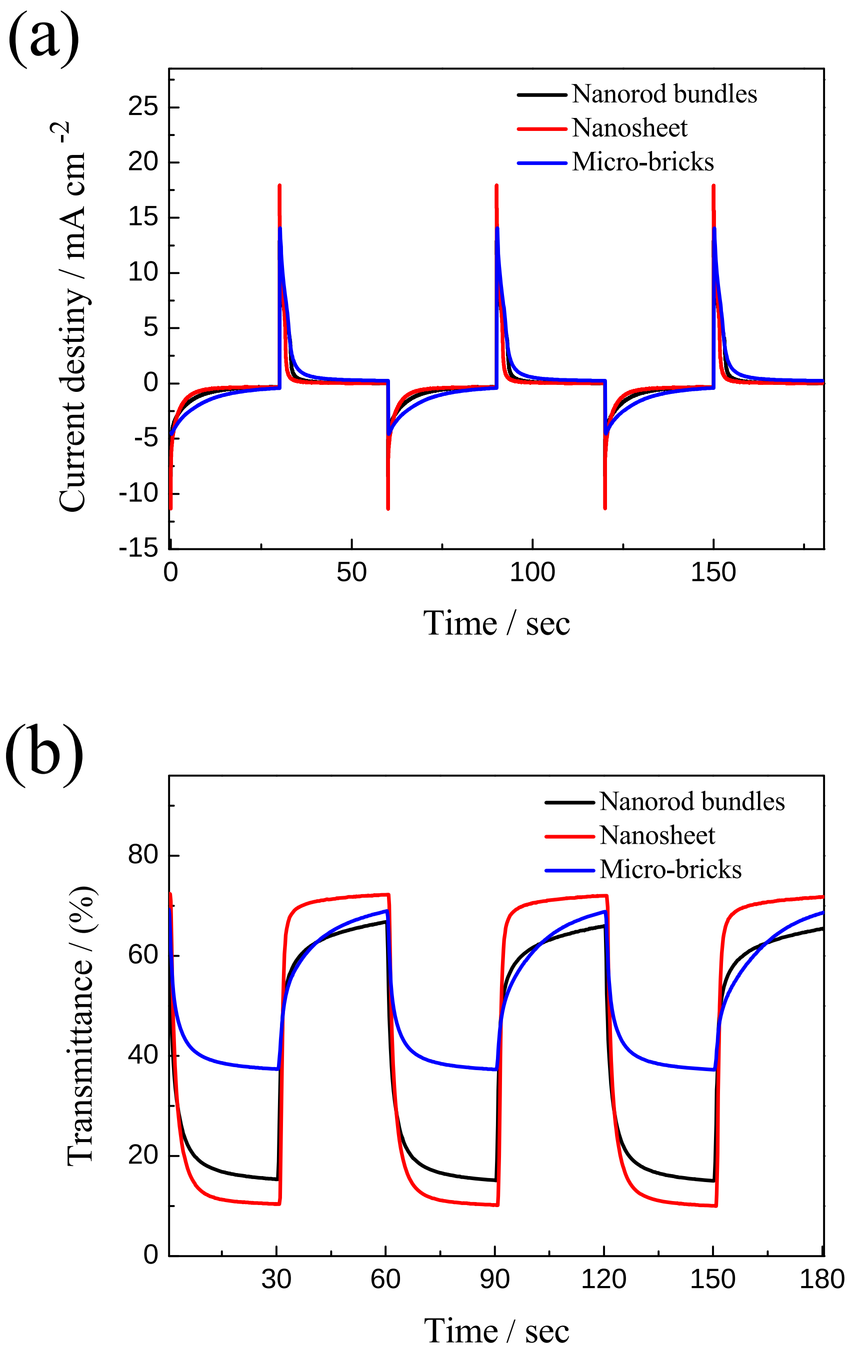
(a)
Nanorod bundles
Nanosheet
Micro-bricks
Current destiny / mA cm -2
25
20
15
10
5
0
-5
-10
-15
0
50
100
150
Time / sec
(b)
Nanorod bundles
Nanosheet
Micro-bricks
Transmittance / (%)
80
60
40
20
0
30
60
90
120
150
180
Time / sec

Fig. 8

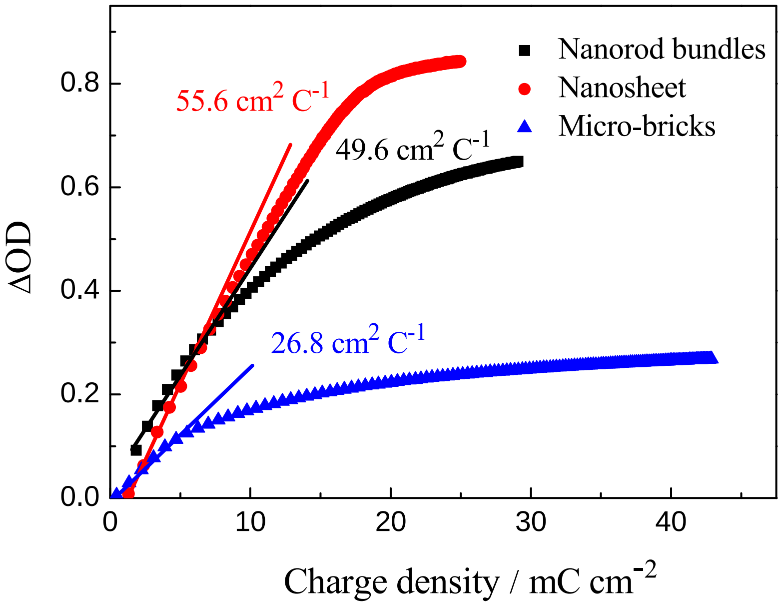
ΔOD
0.0
0.2
0.4
0.6
0.8
0
10
20
30
40
Charge density / mC cm-2
■ Nanorod bundles
● Nanosheet
▲ Micro-bricks
55.6 cm2 C-1
49.6 cm2 C-1
26.8 cm2 C-1

Fig. 9

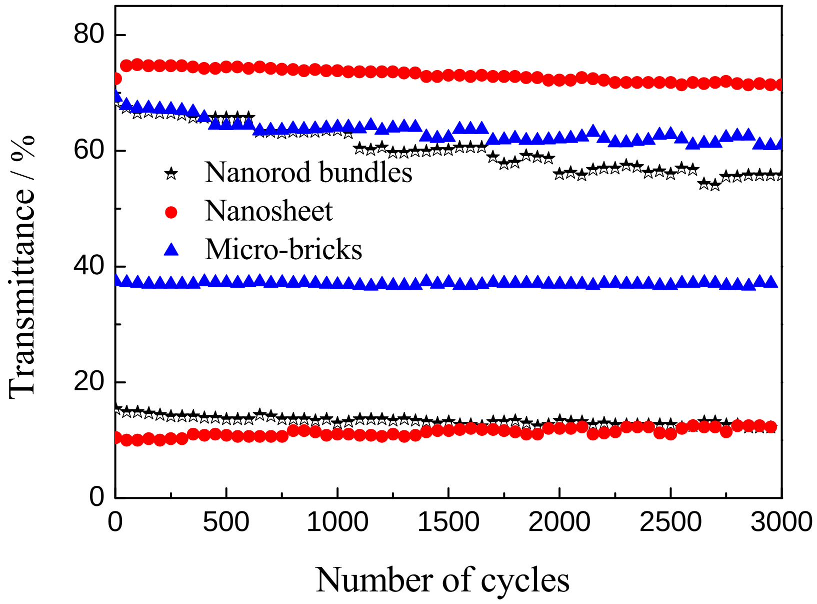
Transmittance / %
Number of cycles
0
20
40
60
80
0
500
1000
1500
2000
2500
3000
Nanorod bundles
Nanosheet
Micro-bricks

Fig. 10

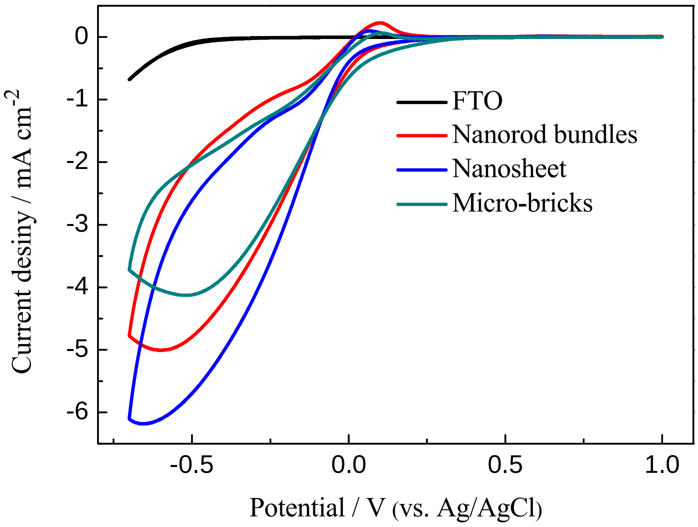
0
-1
-2
-3
-4
-5
-6
Current desiny / mA cm^{-2}
-0.5
0.0
0.5
1.0
Potential / V (vs. Ag/AgCl)
FTO
Nanorod bundles
Nanosheet
Micro-bricks

Fig. 11